MASTER IN QUANTUM SCIENCE AND TECHNOLOGY

Generating arbitrary potentials for Bose-Einstein condensates with a digital micromirror device

Lucía Verdegay Fernández

Supervisors: Rémy Vatré, Leticia Tarruell

ICFO - The Institute of Photonic Sciences

Barcelona, 25.08.2024

Abstract

I detail the development and characterization of an experimental setup capable of generating arbitrary two-dimensional optical potentials using a Digital Micromirror Device illuminated with spatially incoherent light. Spatially incoherent illumination significantly reduces phase-related artifacts, thereby enhancing the quality of the optical potentials. Detailed analyses of the light source and imaging system were conducted to optimize the setup's performance. The results show significant improvements in the homogeneity and sharpness of the potentials compared to those obtained with coherent light. This work lays the groundwork for the final setup, which will be used to trap potassium atoms in the study of the superfluid-to-supersolid transition of a spin-orbit coupled spin-1/2 Bose-Einstein condensate.

Keywords: Ultracold atoms, Bose-Einstein condensate, quasi-2D regime, optical dipole potential, Digital Micromirror Device, spatially incoherent light.

Acknowledgements

I would like to thank Prof. Leticia Tarruell for giving me the opportunity to work in her highly competent group. I would also like to acknowledge my direct supervisor, Rémy Vatré, and the entire K team for their advice and guidance. Thanks to the QGE group, not only for their support and help but also for all the good moments we shared. Finally, I am truly grateful to the ICFO community for their work. It has been a pleasure to be a part of it.

Contents

1 Introduction

When Richard Feynman proposed the concept of a quantum simulator in 1982, he revolutionized the study of quantum many-body physics by suggesting the use of a highly-controlled quantum system to simulate another [1]. Feynman's idea came true thanks to advances in the field of ultracold atoms. Breakthrough achievements, like the creation of Bose-Einstein condensates, enabled by advancements in the control of light-matter interactions and atom cooling techniques, have since opened the door to exploring complex quantum phenomena.

Ultracold quantum gases have now become a powerful tool to study complex quantum many-body problems. By tuning atom-light interactions, researchers can engineer these systems not only to probe condensed-matter phenomena such as phase transitions, but also explore entirely new forms of quantum matter.

A recent example is *supersolidity.* In Bose-Einstein condensates (BECs), spin-orbit coupling can give rise to a supersolid phase, a unique state of matter that combines the frictionless flow of a superfluid with the periodic density modulation characteristic of a crystal. In the context of spin-orbit coupled BECs, this phase is know as the stripe phase. Supersolidity results from two spontaneously broken continuous symmetries: U(1) phase for the superfluid and translational for the solid. The stripe phase of a spin-orbit coupled spin-1/2 BEC has been recently observed in situ for the first time in our group [2].

Intriguing questions remain about the role of dimensionality in this phase transition. To control the dimensionality of the system, the three-dimensional cold gas can be confined along one, two, or three directions. This allows the study of 1D and 2D systems, where the role of thermal and quantum fluctuations is enhanced. Achieving two-dimensionality requires strong confinement in the third direction, typically provided by an optical lattice. By using a Digital Micromirror Device (DMD), which consists of arrays of microscopic mirrors that can reflect light in two different directions, we can trap atoms in the 2D plane in arbitrary shapes. This provides a wide range of applications, such as preparing different atomic density profiles. [3].

The main goal of this master's thesis is to build and characterize a setup for creating 2D box-shaped optical dipole traps, which will be used in the final experiment to study the effect of quantum fluctuations on the superfluid-to-supersolid phase transition. To create this potential, we use a digital micromirror device combined with spatially incoherent light obtained with a multimode diode laser and a multimode fiber.

The contents of this thesis are structured as follows: Chapter 2 explains the theoretical background; Chapter 3 details the properties of the laser and the fiber; Chapter 4 is dedicated to characterizing the incoherent beam after the fiber; Chapter 5 evaluates the performance of the imaging system; Chapter 6 analyzes several squared-box potentials; and the conclusions are presented in Chapter 7.

2 Theoretical Background

Alkali atoms are a popular choice for ultracold gases experiments because of their simple electronic structure, which simplifies their laser cooling and trapping. In this case, the setup built during this master's thesis has been designed to create an optical dipole trap in 2D for K atoms.

Optical Dipole Trap

An optical dipole trap relies on the electric dipole interaction that neutral atoms experience with *far-detuned* light, which has a frequency significantly different from the considered atomic transition. This potential depends on the intensity of the light in the atomic plane, I, and the detuning, which corresponds to the difference between the driving frequency and the one of the electronic transition - i.e. $\delta \equiv \omega_{\text{laser}} - \omega_{eg}$. In alkali atoms, the optical transition $ns \to np$ is usually used for cooling and trapping, where n is the principal quantum number, and s and p refer to the electronic states with orbital angular momentum $l = 0$ and $l = 1$, respectively. Spin-orbit coupling gives rise to the well-known D line doublet between the state ${}^2S_{1/2}$ and the states ${}^2P_{3/2}$ and ${}^2P_{1/2}$, resulting in an energy splitting of $\hbar\Delta'_{FS}$. Here, we use the notation ${}^{2S+1}L_J$, with S being the electronic spin, L the electronic orbital angular momentum, and $J \equiv L \oplus S$ the total electronic angular momentum. Additionally, the coupling to the nuclear spin, I, produces hyperfine structure in both the s and p states, with energy splittings $\hbar\Delta_{HFS}$ and $\hbar\Delta'_{HFS}$, respectively. These states are labeled by the total angular momentum $F \equiv J \oplus I$.

The energy splittings follow the hierarchy $\Delta'_{FS} \gg \Delta_{HFS} \gg \Delta'_{HFS}$. Assuming that $\Delta'_{HFS} \approx 0$, we can derive an expression for the dipole potential that accounts for the three-level energy structure. For linearly polarized light, we obtain the potential

$$U_{\text{dip}} = \frac{\pi c^2 \Gamma}{2\omega_0^3} \left(\frac{2}{\delta_{2,F}} + \frac{1}{\delta_{1,F}} \right) I, \tag{1}$$

where the detunings $\delta_{2,F}$ and $\delta_{1,F}$ correspond to the energy splitting between the particular state ${}^2S_{1/2}, F$ that we are considering and the center of the hyperfine splitting of ${}^2P_{3/2}$ and ${}^2P_{1/2}$, respectively. Therefore, the terms in brackets represent the contribution of the D_2 and D_1 line to the dipole potential [4]. The factor preceding the brackets depends on the central frequency (ω_0) and the average linewidth (Γ) of the D line doublet.

We work with blue-detuned light ($\delta_{2,F}, \delta_{1,F} > 0$) so that the atoms will be attracted to the minima of intensity. Thus, we will employ the DMD to generate box-shaped potentials, which present a dark central region for the atoms surrounded by light barriers.

Bose-Einstein Condensate in a quasi-2D regime

The DMD will create an optical dipole trap in 2D, while there will be a vertical harmonic trap in the third direction with a trapping frequency that we will assume to be $\omega_z/2\pi = 10\,\text{kHz}$ in the following. The three-dimensional BEC will be loaded into this trap. There are two types of regimes in 2D, which are characterized by the relation between the vertical thickness of the cloud, given by the harmonic oscillator length $l_z = \sqrt{\hbar/(m\omega_z)}$, and the range of the interactions. For ultracold Bose gases, only low-energy collisions are relevant. Thus, the range of interactions is governed by the s-wave scattering length, a_s. Since the relation $l_z \gg a_s$ is satisfied in our case, we are in the quasi-2D regime, where the collisions can be treated as in 3D. Therefore, the equations of motion of a 3D weakly-interacting Bose gas have to be derived. Then, these expressions will be transposed to a 2D geometry [5]. For the complete derivation of the Gross-Pitaevski equation in the quasi-2D regime, refer to Appendix A.

The resulting expression is

$$\left(-\frac{\hbar^2}{2m}\nabla^2 + \frac{\hbar^2}{m}\overline{g}|\phi|^2 \right) \phi = \mu\phi, \tag{2}$$

where $\overline{g} = \sqrt{8\pi}a_s/l_z$ is the coupling constant, $|\phi|^2 = n$ is the in-plane density, and μ corresponds to the chemical potential. In this regime, the coupling constant depends on the strength of the confinement in the third direction as $\overline{g} \propto \sqrt{\omega_z}$, with ω_z the frequency of the optical lattice. This is in contrast with the 3D case, where the coupling constant is completely determined by the s-wave scattering length.

If the system is at equilibrium and at $T = 0$, our ground state is the solution to the equation (2). Using the Thomas-Fermi approximation, which assumes that the interaction energy is much larger than the kinetic term, we get

$$\frac{\hbar^2}{m}\overline{g}|\phi|^2\phi = \mu\phi \Rightarrow \mu = \frac{\hbar^2}{m}\overline{g}n. \tag{3}$$

With this expression, the chemical potential can be determined by plugging the corresponding values of our system [6]. By assuming some typical values for the variables in equation (3), such as the ones in Table 1, we estimate the chemical potential of our sample: $\mu \approx 114$nK.

Number of atoms	10^5
Side of the squared box	50μm
Frequency of the harmonic trap	10kHz

Table 1: Typical values considered for the chemical potential calculations.

For the atoms to be trapped, the optical dipole potential of the barrier has to be greater than the chemical potential of the atoms. Taking the expression (1), the optical dipole potential can be represented as a function of the intensity in the atomic plane, I. For the calculations, we use the relation $I = P/A$, where P is the final optical power and A is the area of the illuminated zone, which we assume to be squared. Although we will create a dark hole to trap the atoms, the intensity in the atomic plane remains constant regardless of the shape of the potential. This is because the DMD operates by reflecting light away from the imaging path, keeping the intensity the same for any pattern. Thus, the barrier height can be also computed as the intensity when all the light is sent. In Figure 1, the value of the potential is represented as a function of the power for different sizes of the squared illumination. We consider the isotope ^{39}K for the calculations, whose principal properties are detailed in reference [7]. This plot determines the possible combinations of power and sizes for the initial illumination.

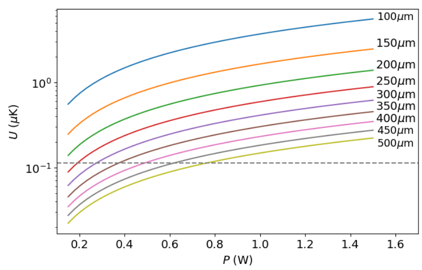

Figure 1: Potential curves. The dashed line represents the chemical potential.

Introduction to the DMD experimental setup

Having established the theoretical framework, let us detail the experimental setup to generate potentials using a DMD. We will work in an object-plane configuration: the pattern generated on the DMD[1] is mapped directly onto the image plane, where the atoms would be. As a first

[1] DLP3000 from Texas Instrument

approach, we initially set up an optical system with coherent illumination, utilizing a single-mode laser diode[2] and a single-mode polarization-maintaining fiber[3]. The setup after the fiber is depicted in Figure 2a.

The optical system labeled D2 images the DMD pattern. It consists of two singlets[4], with focal lengths $f_1 = 150\,\text{mm}$ and $f_2 = 50\,\text{mm}$, and a camera[5]. The first lens is positioned at a distance of f_1 from the DMD. The second lens is located at a distance of $f_1 + f_2$ from the first lens, with the camera positioned at a distance of f_2 from the second lens. In this so-called *4f configuration*, the image of the DMD is demagnified by a factor of f_2/f_1 so that the entire pattern can be captured by the camera. Since the horizontal size of the rectangular chip of micromirrors (6.57mm $\times$ 3.70mm) is 1.14 times larger than the one of the camera (5.76mm $\times$ 4.29mm), a demagnification of at least 0.88 is needed. For the real experiment, this demagnification will increase by an order of magnitude.

To resize the beam and properly illuminate the DMD surface, a magnification stage labeled D1[6] was necessary. This stage also utilizes a 4f configuration, but in this case $f_2 > f_1$. A detailed analysis of this initial test setup can be found in my internship report [8].

With this relatively simple optical setup, it is possible to generate the optical potentials in the atomic plane.

3 Spatially Incoherent Light

Choosing the appropriate light source is crucial to create smooth and sharp potentials. Using coherent light sources, such as very narrow lasers, can lead to phase-related artifacts, usually known as speckle patterns. This results in an inhomogeneous illumination and blurred edges, as shown in Figure 2b from my internship. To overcome this issue, we use spatially incoherent light obtained by combining a multimode laser with a multimode fiber. By reducing the coherence length and adding randomness in the phase, the interference effects decrease, which smoothens the intensity profile of the potentials.

3.1 Laser characterization

We choose a multimode laser diode[7], with a typical wavelength of $\lambda = 675\,\text{nm}$ and a maximum power of 1.2W. Multimode lasers present a wider spectrum than usual ones. In this case, the minimal and maximum lasing wavelengths are 670 nm and 680 nm when the operation is at a temperature of 25°C.

The outcoming power as a function of the current driving the laser diode is represented in Figure 3a. The obtained value for the threshold current was 0.332 ± 0.014 (A), showing a small deviation from the one from the Data Sheet: 0.35A. To understand completely the light source, it is necessary to analyze the spontaneous emission, relevant mostly under and around threshold. This signal is characterized by a broader spectrum and low power. The photons acquire random

[2]EYP-DFB-0767-00050-1500-TOC03-0005 Toptica Eagleyard, distributed by AMS Technologies

[3]PM630-HP from Thorlabs

[4]LC1715-B and LA1986-B from Thorlabs

[5]Alvium 1800 U-1236

[6]LA1433-B and LA1131-B-ML from Thorlabs

[7]USHIO HL67203HD

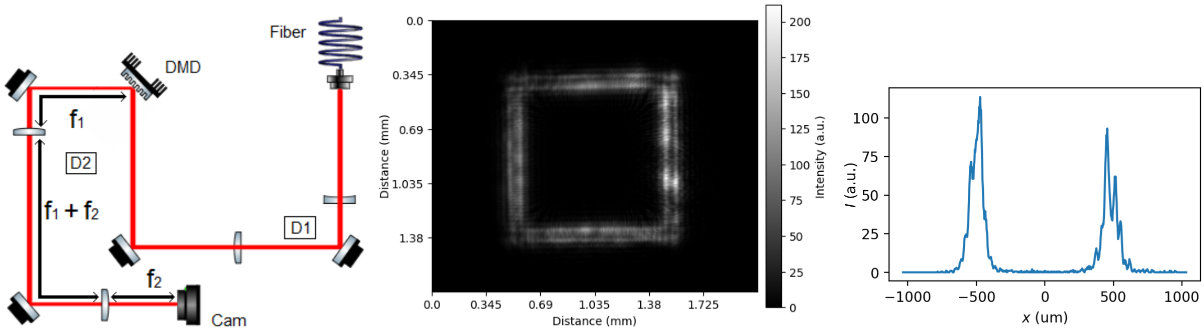

(a) Setup after the fiber. (b) Pattern with coherent illumination. (c) Horizontal cut of the profile.

Figure 2: Results from the tests with coherent illumination [8].

polarizations, which makes the light unpolarized. Its contribution decreases when going above the threshold due to the amplification experienced by the lasing signal for large current values (see Figure 3b).

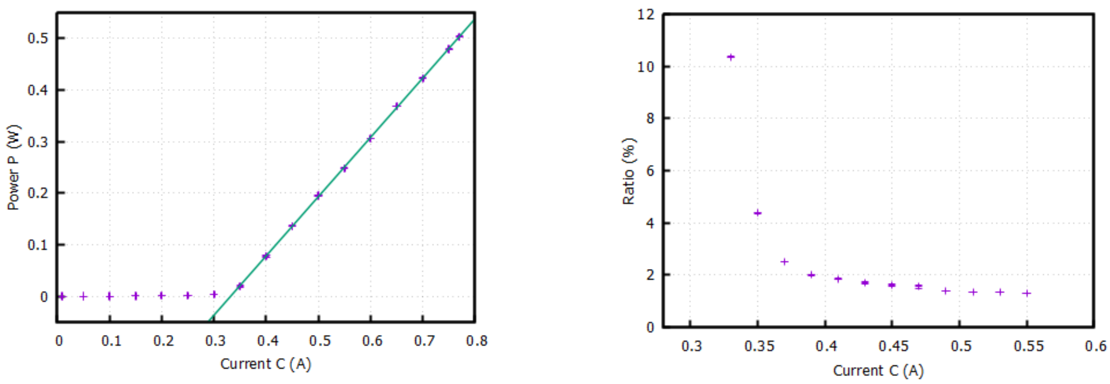

(a) Outcoming power as a function of the current driving the diode laser for a temperature of 25°C. (b) Ratio of the spontaneous emission signal as a function of the current sent to the laser.

Figure 3: Characterization of the multimode laser diode performance.

Due to the high values for the power that the laser can achieve and the danger for eye safety that it represents, I implemented a power dumping stage immediately after the light source. This stage requires two half-wave plates[8] and two Polarization Beam Splitters[9]. To understand the performance of this stage, it is essential to note that the lasing part of the outcoming light is predominately linearly polarized, while the spontaneous emission is unpolarized. Unpolarized light can be described as a mixture of two independent oppositely polarized streams, each with half the intensity [9].

Let us now examine the different elements of the stage (see Figure 4a). A half-wave plate rotates linearly polarized light to any desired orientation. Therefore, the first waveplate changes the polarization angle of the lasing light while leaving the spontaneous emission unchanged. After passing through the waveplate, the light encounters a polarization cube beam splitter,

[8]WPMH05M-670 from Thorlabs and a half-wave plate for 698nm from FOCtek

[9]PBS5204–650-850nm-12.7x12.7x12.7mm from FOCtek.

which transmits only P-polarized light (polarization with the electric field parallel to the plane of incidence). By adjusting the angle of the first waveplate, the amount of lasing light passing through the cube can be controlled, though half of the spontaneous emission is always removed. With this first beam splitter, we ensure that the light is fully linearly polarized from this point onward. Thus, by using the second waveplate to modify the polarization angle, we can control the amount of power exiting the final cube.

The stage is placed inside a box made of anodized aluminum for safety reasons. I designed it with two rectangular holes for the cables of the temperature and current controllers[10], and a circular hole for the light to exit. The sizes of the panels and profiles were chosen so that both the laser and the dumping stage fit inside the box. I also added a slidable top panel made of cellulosic resin to the design for a more comfortable access to the optics inside.

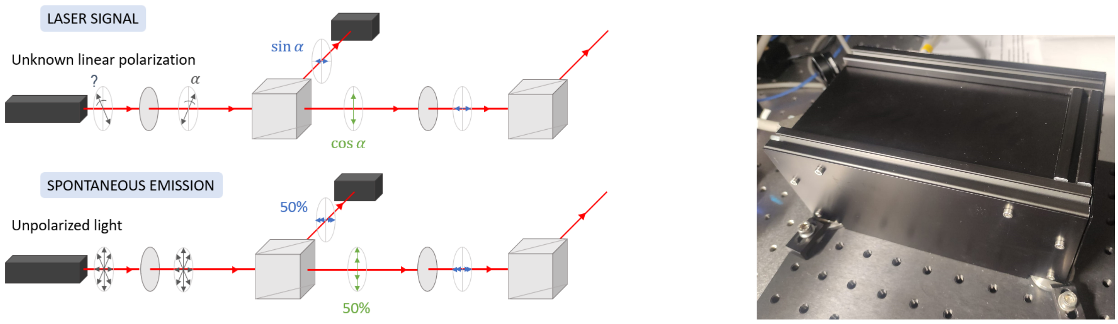

(a) Sketch of the power dumping stage. (b) Laser safety box.

Figure 4: The optical power control stage and the safety box.

3.2 Beam shaping and collimation

Once the diode laser is characterized, it is necessary to reshape and collimate the beam before entering the fiber. The initial shape of the beam was mainly rectangular, although the spontaneous emission is also present as a halo around due to the photons leaving in a broader range of directions (see Figures 5a and 5b). Before entering the fiber, the shape of the beam should be as symmetric as possible. A symmetric beam ensures that light is evenly distributed across the fiber's core, maximizing the amount of light that enters the fiber and minimizing losses.

Firstly, I measured the vertical and horizontal divergence (θ_y and θ_x) by taking images of the beam at different distances from the laser, obtaining $\theta_y = 12.11°$ and $\theta_x = -1.287°$. Thus, the beam is converging horizontally while diverging much faster vertically.

Since the beam at 100mm from the laser has an approximately squared shape, I placed a spherical lens of 125mm focal length[11] at that distance to collimate the vertical direction and make the horizontal one converge faster. Then, to maintain the squared shape, I added a cylindrical lens of $f = -50$mm focal length[12] at 40mm from the spherical one to collimate the horizontal direction (see Figure 5c). With this configuration, a shape close to a square is obtained for our beam.

[10] ITC 4005 controller from Thorlabs

[11] LA1986-B from Thorlabs

[12] LK1662L1-B form Thorlabs

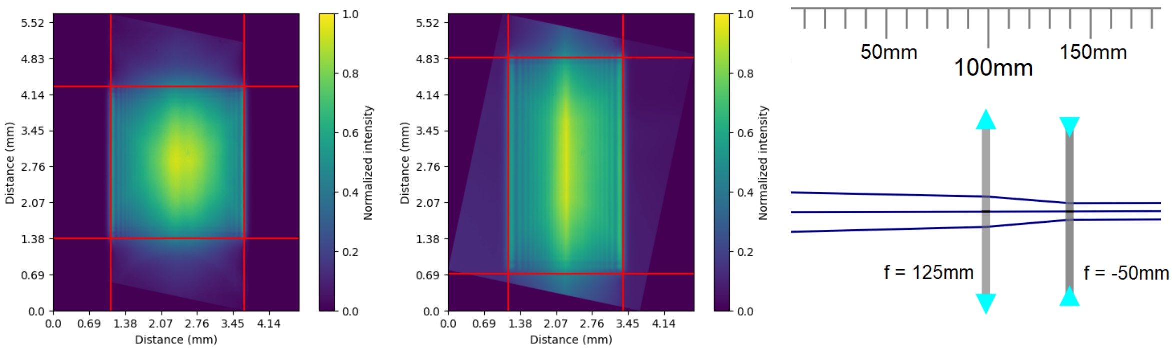

(a) Beam at 13cm from the laser. (b) Beam at 20cm from the laser. (c) Horizontal collimation sketch.

Figure 5: Beam at different distances from the laser.

3.3 Fiber coupling

Combining a multimode fiber with our multimode diode laser, it is possible to get spatially incoherent light for the optical dipole potentials. Since multimode fibers present a spectrally and spatially dependent propagation speed, a time delay between modes is created when light from the laser enters. If this time delay at the end of the fiber is greater than the coherence time of the light source, interference between modes is no longer possible, reducing the spatial coherence. Therefore, for the conversion from temporal to spatial incoherence to be efficient, $\Delta t \gg \tau_t$ has to be fulfilled, where τ_t is the coherence time of the light source and Δt is the modal delay of the fiber.

We use a step-index fiber[13], whose modal delay is given by

$$\Delta t = \frac{\mathrm{NA}^2 L}{2cn_{\mathrm{core}}} = 869.5\,\mathrm{ps} \tag{4}$$

where $L = 5$m is the length, NA$= 0.39$ is the numerical aperture, $n_{\mathrm{core}} = 200$µm is the core size, and c is the velocity of light in vacuum. We are interested in using a long fiber with a high NA to maximize the modal delay. Assuming that the spectrum of the laser diode can be approximated by a Gaussian, the coherence time depends on the Full Width at Half Maximum (FWHM) as [10]

$$\tau_t = \frac{\sqrt{8\pi \ln 2}}{\mathrm{FWHM}}. \tag{5}$$

From the specifications of the laser, a possible value for the FWHM can be estimated as half the difference between the maximal and minimal wavelength. Changing to frequency,

$$\Delta\nu = \frac{c}{\lambda^2}\Delta\lambda = 3.29\,\mathrm{THz}. \tag{6}$$

Therefore, $\tau_t = 1.27\,\mathrm{ps} \ll \Delta t$ is satisfied, ensuring that the conversion from temporally to spatially incoherence is possible.

Regarding the coupling, we need an in-coupler lens that creates a spot size of the diameter of the fiber core. Considering Gaussian optics, the spot size w_f created by a lens of focal length f with an incident beam of size w_0 is of the form

[13] M72L05 from Thorlabs

$$w_f = \frac{\lambda f}{\pi w_0}. \tag{7}$$

Due to the relatively large size of the beam, we choose a lens with a focal length of 15mm[14]. The efficiency of the coupling goes up to 95% thanks to the characteristics of multimode fibers: single-mode fibers only guide the lowest order mode, which is excited by rays with 0° angles of incidence; whereas multimode fibers support multiple propagation modes, meaning that light entering the fiber at various angles can still be guided effectively.

4 Characterization of the beam after the fiber

A Digital Micromirror Device (DMD) is a device formed by arrays of micromirrors (7.6µm size) that can be tilted in two positions: +12° (ON) or -12° (OFF). Therefore, when light is incident onto the surface of the DMD, it can be reflected in two directions. By choosing the micromirrors that are tilted ON or OFF, the creation of different light patterns is enabled.

We use a DMD DLP3000 from Texas Instrument to do the potentials. The rectangular chip of 684x608 micromirrors is illuminated with the incoherent light coming out of the fiber. Thus, it is necessary to characterize and prepare this beam to make sure that the process of creating the potential is as efficient as possible.

4.1 Divergence and shape

When working with Gaussian optics, collimation is related to the Rayleigh length, which is the distance from the waist to where the beam area is twice the beam area at the waist. It is given by $z_{\mathrm{R}} = \pi w_0^2/\lambda$, where w_0 is the beam waist. A Gaussian beam is said to be collimated if the Rayleigh length is much longer than the propagation distance. A spatially incoherent beam of area A_{beam} is formed by randomly distributed Gaussian beams that cover a coherence area $A_c = \pi l_c^2$, where $l_c = c\tau_t$ is the coherence length. The number of these Gaussian beams is given by the ratio A_{beam}/A_c. Then, when the coherence length decreases, more and smaller Gaussian beams are propagating. Since the Rayleigh length is proportional to the square of the beam waist, the divergence increases for very incoherent beams, which are characterized by a small l_c. This makes the divergence unavoidable for our beam source [10].

In this case, the convergence of the beam is characterized by a round-shaped beam with a sharp edge, which corresponds to the image of the fiber core. We want this optimum shape to be at the DMD plane. If the fiber had been square-shaped, it would have been possible to perfectly match the beam with the rectangular chip of micromirrors, illuminating almost all of them without losing power. Using this kind of fiber is the final plan for the experiment. However, due to extended delivery times, it has not yet arrived for testing. We used a fiber with a round core instead, which makes us choose between losing power or letting some mirrors not be illuminated. For our tests, the whole chip was illuminated to characterize the performance of the entire DMD surface, taking the risk of encountering undesired effects due to scattering at the edge of the chip.

[14] AC080-016-A-ML from Thorlabs

4.2 Out-coupler lens

For optical power to be conserved in an optical system, the etendue can never decrease. This quantity is related to how spread out the light is in terms of area and angle. For an infinitesimal surface, $\mathrm{d}S$, crossed by light confined to a solid angle, $\mathrm{d}\Omega$ at an angle θ with its normal, the etendue is defined as

$$\mathrm{d}\xi = n^2 \mathrm{d}S \cos\theta \mathrm{d}\Omega, \tag{8}$$

where n is the refractive index of the medium. Considering an extended source in air emitting light inside a cone of angle α, we get after performing the integral over the surface and solid angle that

$$\xi = \pi A_s (n \sin\alpha)^2 = \pi A_s \mathrm{NA}^2 \tag{9}$$

In a perfect optical system, the etendue of the image is the same as that of the source. The conservation of etendue ensures that the imaging capability of the system is fully exploited [11].

In this case, the fiber acts as the light source, and the potential is the image. To avoid power losses in the optical system, it must be ensured that

$$A_{\text{fiber}} \mathrm{NA}^2_{\text{fiber}} \leq A_{\text{potential}} \mathrm{NA}^2_{\text{objective}}, \tag{10}$$

where A_{fiber} and $A_{\text{potential}}$ are the areas of the fiber core and the created potential, respectively. If the equality holds, we also ensure that the imaging potential of the system is maximally utilized. Thus, the out-coupler lens that images the fiber core onto the DMD surface should not compromise the etendue conservation by being a restrictive element for the NA.

The NA is not the only decisive property in the choice of the out-coupler lens. The beam diverges rapidly, and the image must be formed at a relatively large distance, specifically on the DMD plane. Thus, according to Gaussian optics, the lens must have a sufficiently large focal length. Since they maintain a high NA (0.6) with a large focal length ($f = 20$mm), we used a condenser lens[15].

4.3 Inhomogeneities in the intensity profile

In Section 3, we have concluded that the conversion of temporal to spatial incoherence after the fiber is possible. However, some speckle patterns appear in the intensity profile of the imaged fiber's core. This phenomenon is more evident when increasing the lasing. Under threshold, the spontaneous emission contribution broadens the spectrum of the total signal, and the light is less coherent after the fiber. However, when lasing starts to predominate, the spectrum narrows and the light becomes more coherent, causing these inhomogeneities to appear in the beam profile (see Figure 6). This suggests that the temporal incoherence of the laser diode is not enough to remove all the speckles with this fiber. Therefore, either a light source with a broader spectrum or a multimode fiber with a larger modal delay would be necessary to achieve this.

The speckle patterns are also very sensitive to a change in the angle of incidence into the fiber. This makes acousto-optic modulators and deflectors potential tools to mitigate the inhomogeneities of the beam profile. By sending sound waves through a crystal, the light is diffracted at different angles depending on the frequency. If this frequency oscillates rapidly enough that the atoms cannot notice the changes in the pattern, they will experience the average potential. This also results in a more uniform intensity profile on the camera due to its frame rate.

[15] ACL2520U-B from Thorlabs

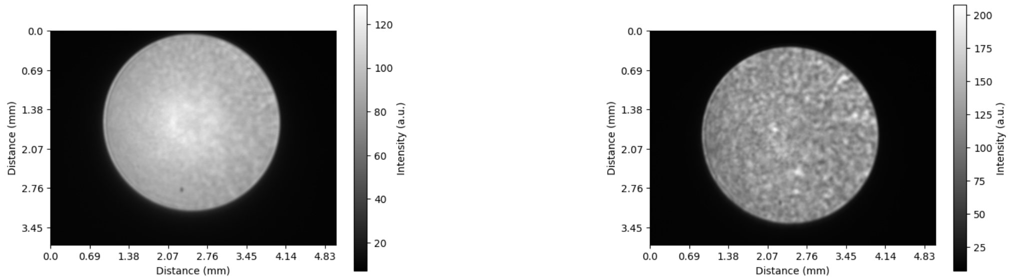

Figure 6: Intensity profile of the focalized beam after the fiber. **Left**: 0.33A of driving power. 3.81% relative standard deviation. **Right**: 0.65A of driving power. 10.15% relative standard deviation

We first placed an acousto-optic modulator[16] (AOM) before the fiber. It has a clear aperture of 1mm, which is large enough for the squared beam, but too small for the entire halo resulting from spontaneous emission. We also tried a 2D acousto-optic deflector[17] (AOD), even if it is not designed for our wavelength. Its aperture is larger in this case, 7.5mm x 7.5mm, and it can deflect vertically and horizontally. AOMs and AODs operate based on the same fundamental principle of acousto-optic interaction, where acoustic waves influence the properties of light. However, their applications differ significantly. AODs are primarily used for deflecting light paths, enabling precise control of beam direction. When used together in a 2D configuration, they can provide accurate control over both horizontal and vertical deflection. In contrast, AOMs are typically employed to modulate the intensity and frequency of lasers, which is essential in many optical setups. While modulation is their primary function, AOMs can also work as deflectors. Thus, it is worthwhile to test both to determine which one performs better in our case.

We align the AOM to maximize the power of the first diffraction order. For the 2D AODs, we use the 1-1 order, which is the first-order diffraction from the first AOD that is then diffracted by the second AOD. After coupling the corresponding order to the fiber, the intensity profile of the beam was measured while changing the amplitude of the oscillations of the driving frequency (see Figure 7). We employed a Voltage Controlled Oscillator (VCO)[18] to convert a DC input voltage into a radio frequency (RF) signal. The RF frequency output of the VCO is directly related to the input voltage. This VCO is driven by an arbitrary waveform generator[19], which produces ramped voltage signals. Consequently, the VCO's output frequency oscillates with the modulation frequency of the input signal. When setting the modulation frequency, it is crucial to ensure that it does not coincide with any resonant frequencies of atomic heating mechanisms. For trapped atoms, these resonances are typically lower than the chosen value: 100kHz.

To compare the performance of both devices, let us consider the mean value and the relative standard deviation of the profiles. Both AOMs and AODs have a center frequency at which the efficiency of the first-order diffraction is maximized. As the modulation amplitude increases, more power is lost due to both the acousto-optic deflector working far from its center frequency, and the change in the angle of incident affecting the fiber coupling. For a detailed analysis of these losses, see Appendix B. At the same time, the relative standard deviation decreases due to more averaging in the profile. The initial relative standard deviation depends on the speckle pattern

[16] ATM-2001A1 from IntraAction

[17] DTSXY-400-1064 from AA

[18] VCO ROS-400 for the AOM and ROS-150 for the AODs from ICFO electronic workshop

[19] SIGLENT SDG6032X

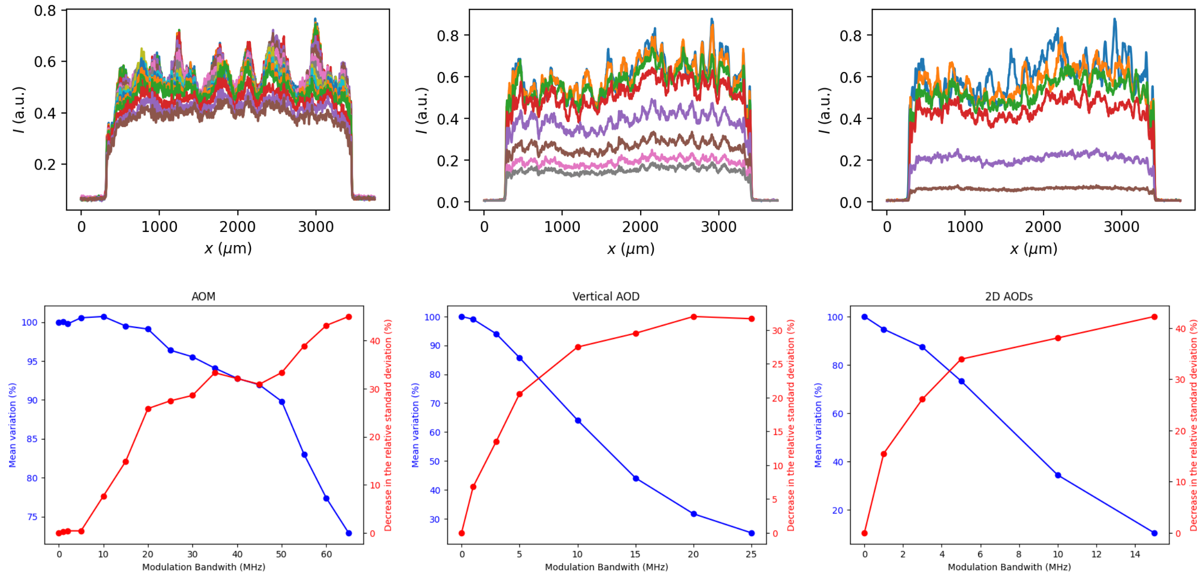

(a) AOM (b) Vertical AOD (c) 2D AODs

Figure 7: Comparison of the profiles for different modulation amplitudes of the oscillations.

of the beam at the time of measurement. This value is different for the AOM and the AODs analysis because the initial angle of incidence was not the same for both measurements. Thus, using the difference of the standard deviation relative to each initial value is more convenient for comparison.

In Figure 7, the mean intensity variation and the decrease in the relative standard deviation are plotted as a function of the modulation bandwidth. Using the AOM, we achieved a 30% reduction in the relative standard deviation with losing only slightly more than 5% of intensity. Then, we tried to modulate the frequency of the vertical AOD while keeping the horizontal AOD at its center frequency. In this case, to achieve a similar 30% reduction in the relative standard deviation, the mean intensity is reduced to 45% of its initial value. We also modulated the frequency of both AODs simultaneously. This approach did not perform as well as the AOM either: losses were up to 20% for a 30% reduction. Nevertheless, none of the setups could be useful in the conditions of the test due to the low power efficiency obtained. For the first diffraction order of the AOM at the test RF power, the efficiency was less than 10%, which is much lower than the 90% expected. Approximately the same power was obtained for the 1-1 order of the AODs. Due to the time constraints associated with these tests, an extended analysis of the potential efficiency improvements through increasing RF power has yet to be conducted. The contribution of the incoherence of the light source to this issue should be also quantitatively determined.

5 Quality of the imaging system

The optical system for imaging the DMD consists of two lenses, with focal lengths f_1 and f_2, and the camera. Using a 4f configuration, the image of the DMD is demagnified by a factor of f_2/f_1 and captured by the camera, which is positioned where the atoms would be trapped. To avoid artifacts due to reflections on a tilted surface, the beam after the DMD should leave perpendicular to its surface. By setting an incident angle of $\pm 24°$ with respect to the surface, the micromirrors tilted $\pm 12°$ are imaged in the plane of the camera, letting us visualize the pattern sent to the DMD. To ensure the angles were correct, I first placed the DMD so that its front surface was parallel to the reference grid of the optical table. Then, I set all the micromirrors to a $-12°$ tilt and aligned the incident beam so that the reflection was perfectly perpendicular to the DMD surface. This ensured that the incident angle was $-24°$.

5.1 Analysis of the Point Spread Function

A critical feature for characterizing the imaging system is the resolution, which determines the minimal distance between two points of the object plane that can be seen independently in the image. Even for a perfect optical system with no aberrations, the finite aperture limits the possible resolution and is the so-called diffraction limit. The far-field condition ensures that the distances in an optical system are such that the angular distribution of the light becomes nearly uniform, and the effects of curvature of the wavefront can be ignored. If all distances in the assembly are such that the far-field assumption is valid, the image of a point source - the point-spread function (PSF) - can be well described as an Airy disk, i.e.

$$\mathrm{PSF}(r) = A\left(\frac{J_1(\alpha r)}{\alpha r}\right)^2, \tag{11}$$

where J_1 is the Bessel function of the first kind of order one, and A and α are variables related to the characteristics of the system. Considering the Rayleigh criterion, which states that two points are still distinguishable if the central maximum of the first Airy disk directly overlaps with the first diffraction minimum of the second disk, the expected resolution for a diffraction-limited system is given by

$$R = 0.61\frac{\lambda}{\mathrm{NA}}, \tag{12}$$

where the limiting NA of the optical system is considered. Therefore, by fitting the PSF from the optical system to an Airy disk, the resolution can be computed using the extracted width. However, due to the complexity of Airy disk fits, a 2D Gaussian function can be used instead to directly determine the resolution. A 2D Gaussian is of the form

$$G(x,y) = C\ \exp\left(-\frac{(x-x_0)^2}{2\sigma_x^2}\right)\ \exp\left(-\frac{(y-y_0)^2}{2\sigma_y^2}\right), \tag{13}$$

where C, x_0, y_0, σ_x and σ_y are free parameters in the fit. According to [12], the resolution is given by $R = 2.905\sigma$.

As a first approach to imaging the DMD, we used a couple of singlets[20]. It was particularly useful to test the first patterns and images of the PSF. Due to the aberrations that these lenses introduce, they are not suitable for a high quality imaging system. Then, we changed them for achromatic lenses[21], which are designed to limit the effects of aberrations. In this case, the diameters and the focal lengths of the achromats are larger than for the singlets, ensuring a larger aperture and the fulfilling of the far-field assumption. Figure 8 shows the two setups.

[20] LA1509-A and LA1433-B from Thorlabs

[21] ACT508-500-B and ACT508-400-B from Thorlabs

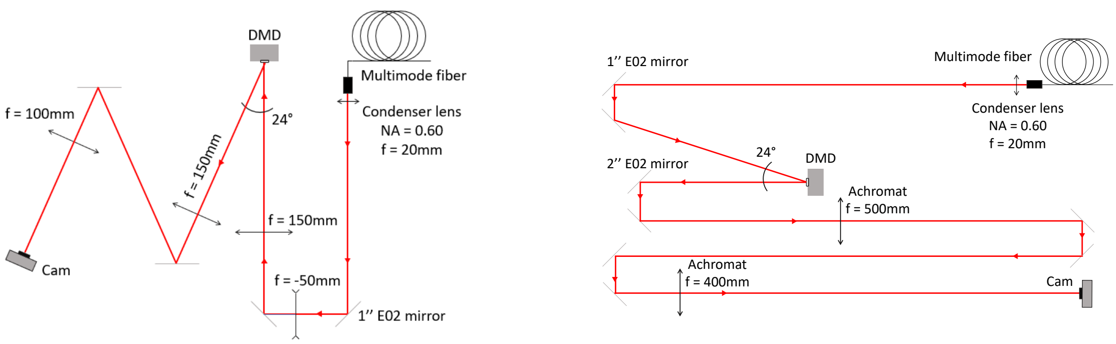

(a) Singlets setup. A telescope before the DMD was needed to make the beam size suitable for illuminating the DMD surface (LC1715-B and LA1433-B from Thorlabs). The 1'' mirrors are BB1-E02 from Thorlabs.

(b) Achromats setup. A cage system for the first lens and a translational stage for the camera are set due to the high sensitivity of the alignment to a change in these distances. The 2'' mirrors are BB2-E02 and BBE2-E02 from Thorlabs.

Figure 8: Different setups for the comparison of the resolution.

We consider a single micromirror as a point source, as it represents the smallest discrete unit of light emission in our system. For the point source approximation to be valid, the size of the micromirror, multiplied by the demagnification factor, must be significantly smaller than the expected resolution of the imaging system. For this DMD, each micromirror is 7.6µm in size. The demagnification factors are 0.67 for the singlets and 0.8 for the achromats, ensuring that the entire DMD surface is imaged within the camera. This implies that each micromirror corresponds to one or two pixels. According to equation (12), the expected resolutions are 4.9µm and 8.1µm for the singlets and the achromats, respectively. Thus, a single micromirror cannot be considered as a valid point source, and its shape affects the PSF. For a detailed analysis of these effects, see Appendix C, which concludes that the Gaussian convoluted with the image of a micromirror constitutes a suitable fitting function to compute the resolution.

To study the PSF of both optical systems, we use a pattern where a single micromirror is sending light at each vertex of a 40x40 mirror square. This repeats across the entire DMD surface, creating a grid of illuminated points (see Figure 9). Using this configuration, we analyze the imaging quality across different zones of the DMD surface.

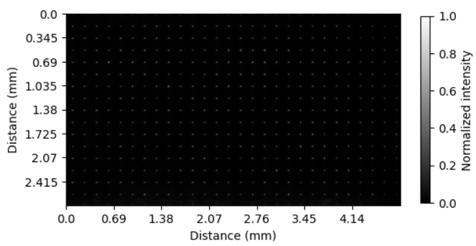

Figure 9: Image of the periodic pattern.

In Figure 10, the size of the PSF obtained by the fitting process are plotted as a function of the distance from the center of the DMD for both singlets and achromats setups. For this comparison, we consider the actual demagnification of each setup, which can be also obtained from the images of the periodic PSF. By knowing the distance between the light-sending mirrors on the DMD and measuring the separation between the centers of the PSFs in the image, the demagnification is calculated as the ratio of these two distances.

With the singlets, the PSF gets worse when getting further from the center, specially horizontally. In contrast, the PSF is almost unperturbed along the DMD surface for the achromats case. It is also worth remarking that the horizontal width is larger than the vertical one, which implies that the PSF is not completely symmetric.

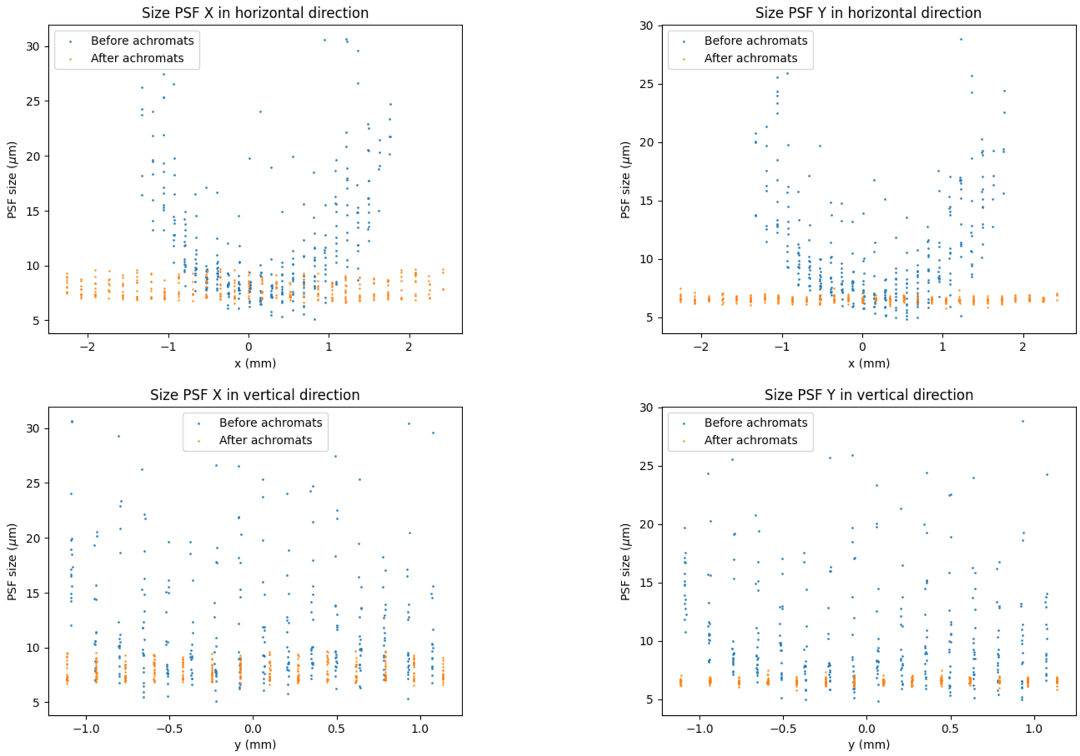

Figure 10: Values of σ_x and σ_y obtained by fitting each PSF to a Gaussian convoluted with the image of a micromirror. The horizontal axis represents the distances from the center of the DMD image in each direction.

From the results of the fits, we compute the resolution as $R = 2.905\sigma$. We compare the diffraction-limited resolution obtained with equation (12) and the resolution from the fits in Table 2. As a criterion, the value of R_{fit} is selected as the one with the highest frequency in the histograms of Figure 11. They represent the vertical resolution values with a step size of 0.1µm.

	R_{Rayleigh}	R_{fit}	Ratio
Singlets	4.9µm	15.4µm	3.1
Achromats	8.1µm	17.6µm	2.2

Table 2: Values for the resolution.

Although the resolution ratio, defined as $R_{\text{fit}}/R_{\text{Rayleigh}}$, is higher for the singlets setup than for the achromats one, the results with the achromats are still worse than expected. If the full aperture of the lenses is not utilized, the theoretical resolution is overestimated because it assumes that the lens diameter is the limiting factor. This discrepancy is related to the non-conservation of etendue. While etendue does not decrease, ensuring no power losses, it differs between the source and the image. As a result, the imaging capability is not fully exploited,

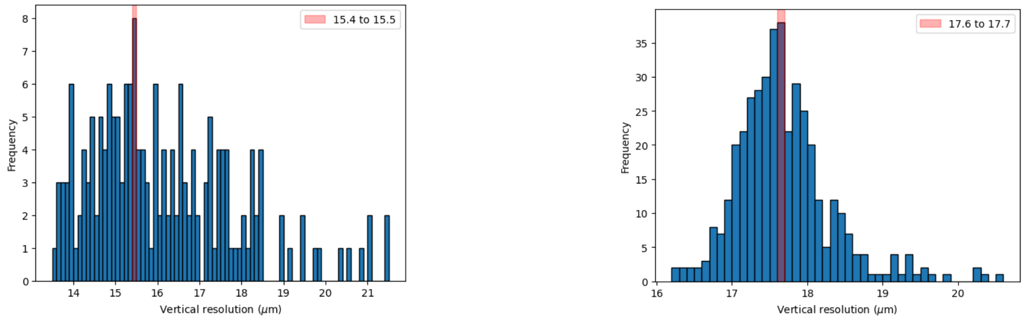

(a) Singlets.

(b) Achromats.

Figure 11: Histogram of the vertical resolution with $0.1\mu\mathrm{m}$ step size.

leading to reduced resolution. Determining how much of the aperture is used for imaging can help us estimate a more realistic resolution for this optical system. To address this, we studied the effect of closing an iris just before the lenses on the PSF. In Figure 12, the relative variation of PSF size is represented as a function of the aperture.

The horizontal PSF size remains approximately constant until the aperture reaches 25 mm, at which point it decreases before increasing again at 15 mm. This behavior suggests both that only around 25mm of the aperture is being used, and that cutting the edges of the beam might be beneficial, specially for the horizontal direction. The edges of the beam could be adding aberrations that affect the PSF quality. Considering 25mm of aperture in the expression for the resolution, $R_{\text{Rayleigh}} \approx 16.5\mu\mathrm{m}$, which is a value much closer to the one obtained with the fitting.

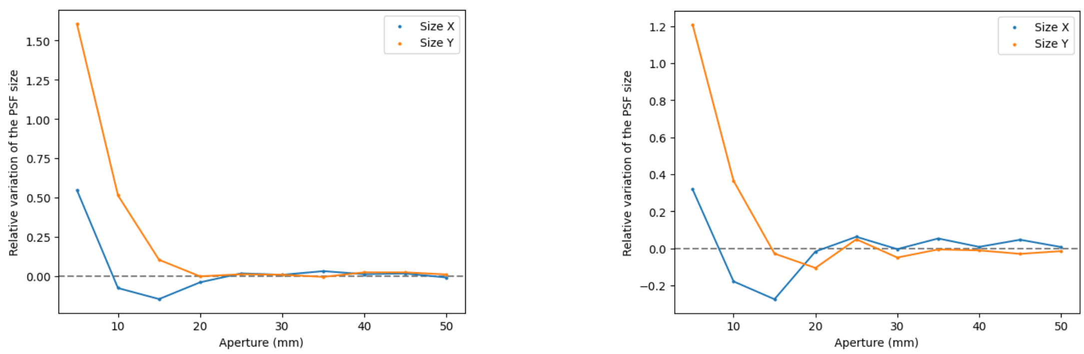

(a) 3" iris placed just before the first lens.

(b) 3" iris placed just before the second lens.

Figure 12: Relative variation of the PSF width as a function of the aperture size.

At this point, due to the high dependence of the PSF on the position of the camera (see Figure 13), finding the focus is key for characterizing the performance of the imaging system. As a criterion, the PSF with a higher Strehl ratio will be considered to be in the focus. The Strehl ratio corresponds to the ratio between the peak intensity of the aberrated Airy disk and the ideal one. If it is larger than 0.8, the system can be considered diffraction limited. Since all images are normalized to their maximum intensity, computing the Strehl ratio involves integrating both the imaged PSF and the expected Airy disk. The peak intensity for each case is given by the inverse of the respective integrals. The Strehl ratio is then obtained by taking the ratio of these peak intensities.

The Strehl ratio reached its maximum value, 0.438, for the starting point in Figure 13. This result not only establishes a focus, but also ensures that the diffraction limit has not been achieved. However, a relevant aspect when analyzing the Strehl ratio is that one micromirror cannot be considered as a point source in this imaging system. Consequently, what we interpret as a PSF deviates from an ideal Airy disk, potentially influencing the Strehl ratio results.

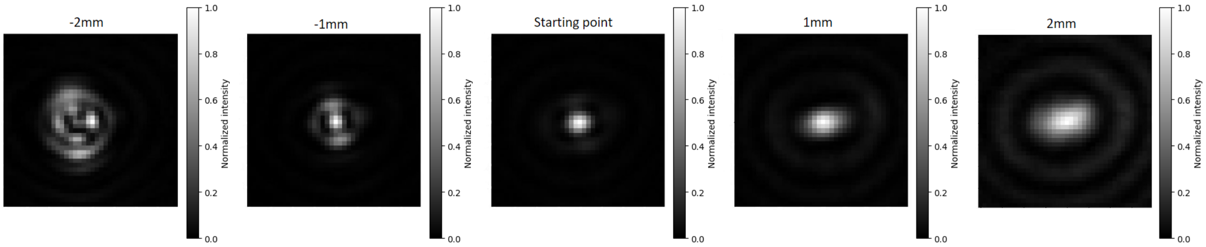

Figure 13: PSF for different longitudinal distances of the camera. Images of 138µm × 138µm.

Although we have established the focus by considering the best Strehl ratio, the focalization seems different when imaging larger patterns. As shown in Figure 14a, the edges of the bright square of 20 micromirrors side are much sharper for the position of the PSF with a smaller Strehl ratio than for the focus. This implies that the focus for imaging larger patterns would be different than the focus for the PSF. One possible explanation would be that imaging a larger portion of the DMD can benefit from spatial incoherence, which reduces phase-related artifacts and improves image quality at a specific distance. This averaging effect resulting from the lack of interference is influenced by the illumination of multiple micromirrors. In contrast, when imaging a single micromirror, phase randomness can create irregular patterns that affect the PSF width at that specific position. Supporting this hypothesis, the inverse pattern of the PSF - i.e., where only one micromirror is not illuminated - shows a narrower width compared to the direct pattern, as illustrated in Figure 14b.

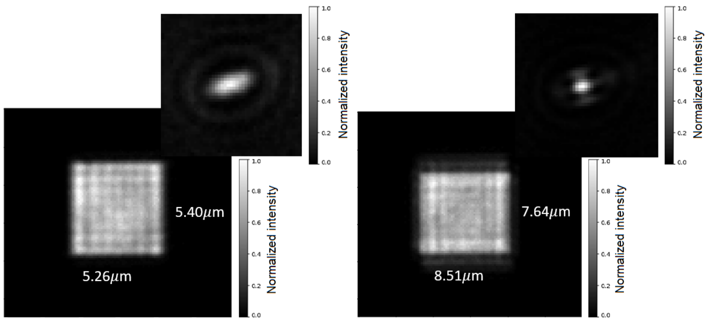

(a) Sharpness of the edges of a bright square of 20 micromirrors for two different longitudinal positions of the camera.

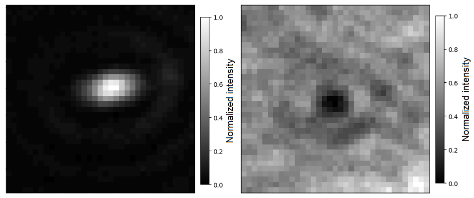

(b) Inverse pattern of the PSF. Images of 138µm × 138µm.

Figure 14: Analysis of the sharpness of the edges and the inverse pattern of the PSF.

The negative effect on the PSF seems more evident in the horizontal direction, maybe due to the angle of incidence on the DMD. The incident-light path is forming 12° relative to the micromirrors in the horizontal direction, which means that the optical path length across the micromirror varies between the edges. This variation could be introducing even more randomness in the phase, resolving to be worse horizontally than vertically.

5.2 Depth of field and depth of focus

The depth of field is defined as the range of longitudinal distances (i.e. distances along the propagation direction) within the object space where objects are imaged with acceptable quality, whereas the depth of focus constitutes the range of longitudinal distances within the image space where the camera can be moved while maintaining acceptable sharpness. Both provide useful information about the performance of an imaging system. To measure these quantities, the size of the PSF is represented as a function of the displacement from the focus in Figure 15.

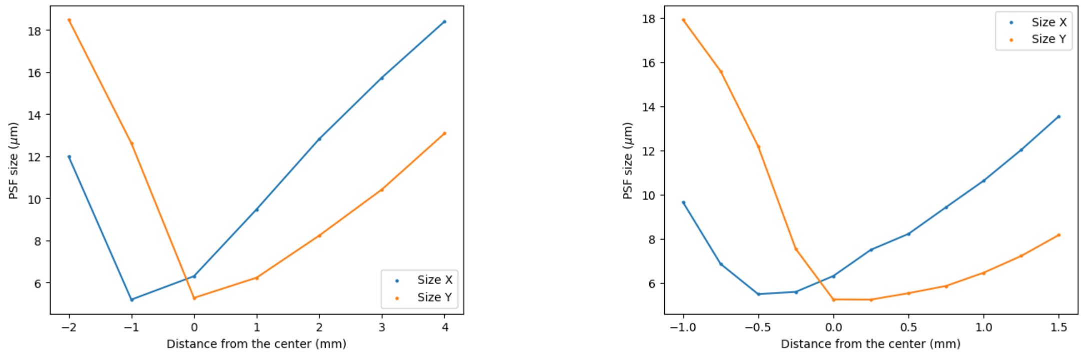

(a) Depth of field. (b) Depth of focus

Figure 15: Size of the PSF as a function of the displacement from the optimum position (a) of the lens; (b) of the camera.

The depth of field of an imaging system is given by

$$\mathrm{DoF} = \frac{\lambda}{(\mathrm{NA})^2}, \tag{14}$$

where NA is the numerical aperture of the objective [13]. In our case, the value is of the order of hundreds of micrometers.

As a qualitative analysis, both plots exhibit asymmetric behavior between negative and positive displacements, which typically indicates the presence of aberrations in the imaging system. Furthermore, the curves for horizontal and vertical sizes are displaced relative to each other, with their minimum values occurring at different positions. This is a clear indication of astigmatism, which could be corrected with specialized optics in the future. These issues make giving concrete experimental values a complicated task.

We define an experimental estimation of the DoF as the distance between the two points where PSF size is 1.5 times its minimum value. By applying linear interpolation to the data, we estimate the depth of field to be approximately 2.1 mm. Considering the same estimation for the depth of focus, the distance is around 1.3 mm. Since this value is significantly larger than $l_z = 161.1\,\mathrm{nm}$ of the harmonic trap, the main conclusion is that the atoms will not experience noticeable defocusing.

5.3 Modulation Transfer Function

The Modulation Transfer Function (MTF) is a measurement of the ability of an imaging system to transfer contrast from the object to the image. To study the MTF of the imaging system, a pattern of periodic lines with several spacings is sent to the DMD, vertically (see Figure 16a) and horizontally. The contrast is computed as

$$C = \frac{I_{\max} - I_{\min}}{I_{\max} + I_{\min}}, \tag{15}$$

where $I_{\max}$ and $I_{\min}$ are the maximum and the minimum of intensity in the line pair (lp), respectively.

In Figure 16b, the contrast obtained from the image of the pattern of periodic lines is represented as a function of the frequency in line pairs per millimeter. For a diffraction-limited system, the behavior should be almost linear. When there exists some defocus, the linear dependence is lost. For spatially incoherent light, the expected cutoff frequency is estimated as

$$\xi_{\text{cutoff}} = \frac{1}{\lambda \cdot F} = \frac{2\text{NA}}{\lambda}, \tag{16}$$

where $F = (2\text{NA})^{-1}$ is the f-number of the limiting lens [14]. In our optical system, $\xi_{\text{cutoff}} \approx$ 135lp/mm.

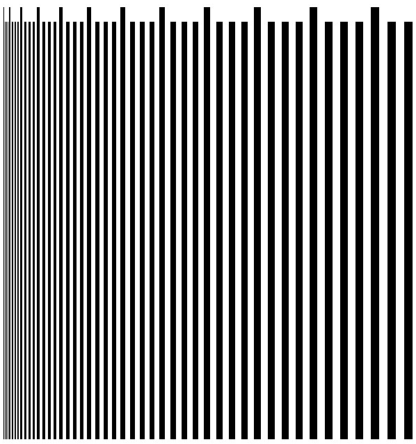

(a) Pattern for measuring the MTF.

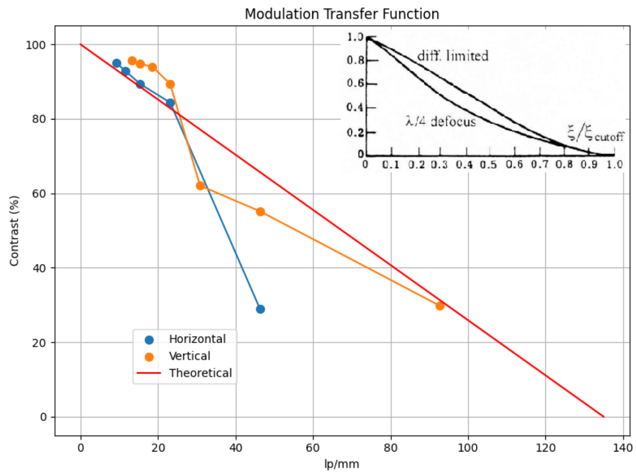

(b) Contrast as a function of the frequency. Upper figure [14]

This result confirms that the system is not diffraction limited, specially horizontally. However, it is hard to come to conclusions when the number of points is too low - the amount of data is limited by the DMD, since the smallest separation possible is a row of micromirrors.

6 Squared box potentials

In the generation of the final square box-shaped potentials, the plan is to use a high NA objective to image the pattern onto the atomic plane. To conserve the etendue, the side length of the square illumination - when the DMD reflects all incident light into the imaging path - must satisfy

$$d_{\text{potential}} = \sqrt{A_{\text{fiber}}} \frac{\text{NA}_{\text{fiber}}}{\text{NA}_{\text{objective}}} \tag{17}$$

Assuming that the numerical aperture of the objective is a value near 0.6, the illuminated area has to be around 115µm × 115µm in the future experiment. This will determine the required demagnification.

Let us focus the following analysis on relevant characteristics of the square box potentials. In particular, we will study the sharpness and the darkness.

Using blue-detuned light is an easy way to create a *flat* zone for the atoms. Since they are attracted to the minima of intensity, they are trapped in the non-illuminated hole of the box. Achieving homogeneous illumination in the optical system is important to ensure that the height of the barriers remains approximately constant along the trap. However, in an optimal trap, the atoms have to experience the same optical dipole potential, making it necessary to characterize how dark the non-illuminated region is. Another relevant characteristic of the potential is the sharpness of its edges. The smoother they are, the further the trap is from the boxed potential considered in the theoretical model. The sharpness can be measured by fitting the intensity profiles to a convolution of a step function and a gaussian, whose σ is related to this feature.

For these analyses, three squared boxes of sizes 10, 20 and 50 micromirrors were imaged. The *non-illuminated* zones can be seen in Figure 17.

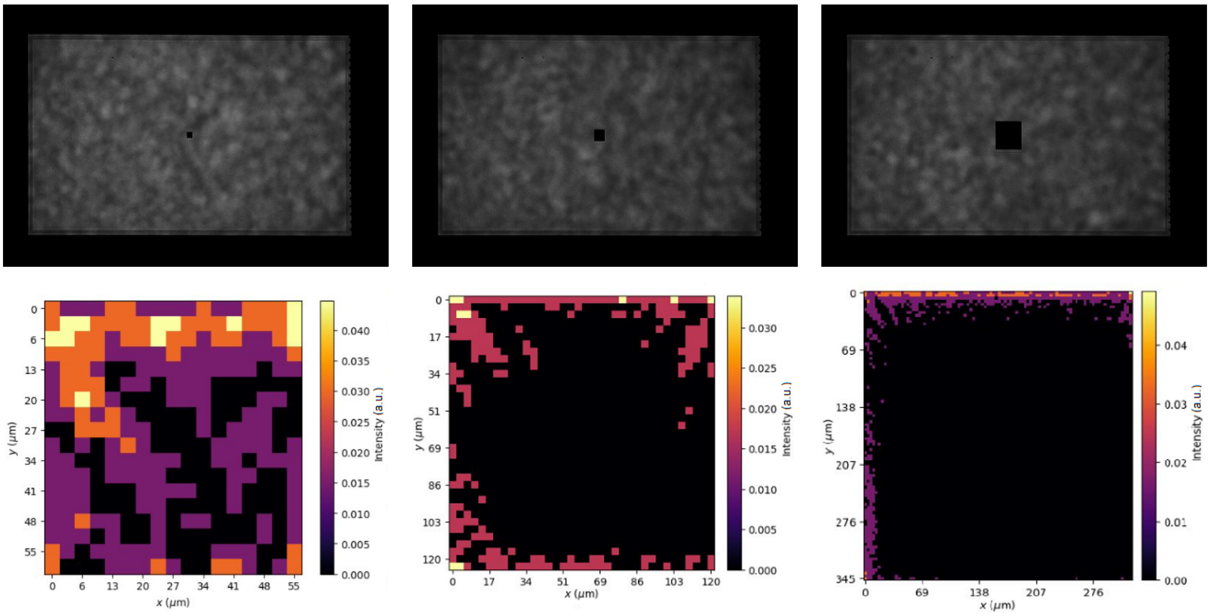

(a) 10 mirrors side. (b) 20 mirrors side. (c) 50 mirrors side.

Figure 17: **Up:** Images (5.8mm x 4.3mm) of the squared boxes. **Down:** Darkness of the holes.

We compute the standard deviation inside the hole relative to the bright region, giving (a) 2.58%, (b) 1.4%, and (c) 1.18%. As expected, the standard deviation decreases as the dark zone enlarges. The sharpness of the barriers behaves differently. We calculate the mean value of the fitted σ from the horizontal and vertical Gaussian fit, resulting in (a) 4.1 µm, (b) 3.9 µm, and (c) 3.3 µm. This indicates that the walls are sharper for larger boxes. Thus, we conclude that it is more convenient to use larger boxes in terms of darkness and sharpness of the potentials. However, the risk of tunneling through the box walls should also be considered as the barriers start to get thinner.

The σ obtained as the sharpness is related to the resolution of the imaging system by the same expression $R = 2.905\sigma$ considered in Section 5. Using the values of the σ discussed before, the resolution is significantly smaller than the results from the PSF measurements. This observation further supports the hypothesis that the optical system performs at a higher quality when imaging larger patterns.

Finally, we compare the sharpness obtained with incoherent illumination to that achieved with coherent light during my internship. I measured a σ of approximately 22 µm using the same fitting process described in this section [8]. Thus, the sharpness and resolution achieved with incoherent light represent an improvement of 667% compared to the results obtained with the coherent illumination setup.

7 Conclusions

In this master's thesis project, I prepared a test setup for creating 2D box-shaped optical dipole potentials using a Digital Micromirror Device illuminated with spatially incoherent light. I characterized its performance and provided useful insights for the final setup that will be used in the experiment.

First, I performed some realistic calculations for the final experiment, obtaining an estimation of the chemical potential of the sample and the optical dipole trap. I also described the conversion from temporal to spatial incoherence using a multimode diode laser and a multimode fiber. I tested the light source and designed a power control stage for it. After shaping the beam, I coupled it into the fiber. Based on the specifications of the multimode fiber, I calculated the efficiency of the conversion from temporally to spatially incoherent light.

Characterizing the beam after the fiber is crucial for preparing the optimal beam that will be incident onto the DMD surface. I imaged the fiber's round core in the DMD plane, ensuring that all the micromirrors were illuminated, though this resulted in some power losses. In the final experiment, the core will be square to better match the rectangular chip of micromirrors. The beam profile showed some speckles, leading us to conclude that the spectrum of the multimode laser was not broad enough to completely eliminate phase-related artifacts when using this multimode fiber. To mitigate this issue, I proposed using acousto-optic deflectors. While the tests showed promising results, further analysis is needed to understand the low efficiency of the first orders.

I designed an imaging system consisting of two lenses to image the DMD pattern onto a camera. I demonstrated the advantage of using achromatic lenses over singlets by comparing the resolution values across the DMD surface. I provided a detailed analysis of the PSF, explaining its relationship with the resolution and the focus. Additionally, I measured the depth of field and depth of focus, as well as the Modulation Transfer Function (MTF) of the optical system. As a final analysis, I studied relevant characteristics of the box-shaped potentials, such as the sharpness of the walls and the homogeneity of the darkness inside the trap.

In conclusion, using spatially incoherent light shows significant improvements over coherent illumination in the quality of the potentials, particularly in terms of homogeneity and sharpness of box-shaped traps. Combining this illumination with a Digital Micromirror Device enables the creation of arbitrary potentials, which have a wide range of applications for ultracold quantum gases experiments. As a follow-up to this work, the setup with the already ordered squared-core fiber and the final objective needs to be prepared. Tests of the performance of two AODs designed for the correct wavelength should also be conducted to determine their suitability for the final setup. Another important task would be measuring the spectrum of the laser to confirm the validity of the estimations made in this master's thesis. Moreover, given the observed speckles in the beam profile, a more temporally incoherent light source, such as a superluminescent diode, could be considered for the experiment.

Bibliography

[1] R. P. Feynman, International Journal of Theoretical Physics **21**, 6 (1982).

[2] C. Chisholm, S. Hirthe, V. Makhalov, R. Ramos, R. Vatré, J. Cabedo, A. Celi, and L.Tarruell, "In situ observation of supersolid dynamics in a spin-orbit coupled Bose-Einstein condensate." In preparation.

[3] Y.-Q. Zou, Le Cerf, B. Bakkali-Hassani, C. Maury, G. Chauveau, P. C. M. Castilho, R. Saint-Jalm, S. Nascimbene, J. Dalibard, and J. Beugnon, Journal of Physics B: Atomic, Molecular and Optical Physics **54**, 08LT01 (2021).

[4] R. Grimm, M. Weidemüller, and Y. B. Ovchinnikov (Academic Press, 2000) pp. 95–170.

[5] Z. Hadzibabic and J. Dalibard, La Rivista del Nuovo Cimento **034**, 0 (2011), lecture notes from the Varenna Summer School, 2009.

[6] C. Maury, *Probing few and many-body physics in a planar Bose gas: Atom-dimer interactions and zero-temperature superfluid fraction.*, Ph.D. thesis, Sorbonne Université (2023).

[7] T. Tiecke, "Properties of potassium," (2019).

[8] L. Verdegay, "Generation of arbitrary potentials for ultracold atoms using digital micromirror devices," (2024), master Internship report. ICFO and Universidad de Barcelona.

[9] H. Prakash and N. Chandra, Physical Review A **4**, 796 (1971).

[10] B. Heizenreder, *Creation of arbitrary potentials with a digital micromirror device. Towards quantum simulation with ultracold polar molecules.*, Master's thesis, ludwig-Maximilians-Universität München and Max-Planck-Institut, (2021).

[11] W. H. Steel, Applied Optics **13**, 704 (1974).

[12] B. Zhang, J. Zerubia, and J.-C. Olivo-Marin, Applied Optics **46**, 1819 (2007).

[13] L. Meihua, L. Dajiang, P. Giancarlo, O. Wolfgang, S. Guohai, H. Wenqi, and P. Xiang, Scientific Reports **9**, 7165 (2019).

[14] G. D. Boreman, *Modulation Transfer Function in Optical and Electro-Optical Systems*, Vol. TT121 (SPIE, 2001) page 156.

A Derivation of the Gross-Pitaevski equation

This Appendix includes the derivation of the 2D Gross-Pitaevski equation starting from the 3D case. Let us consider a 3D dilute gas of $N \gg 1$ identical bosonic atoms, whose interactions can be described by a contact potential

$$U(\mathbf{r}_i - \mathbf{r}_j) = g_{3\mathrm{D}}\delta(\mathbf{r}_i - \mathbf{r}_j), \tag{18}$$

where $g_{3\mathrm{D}} = 4\pi\hbar^2 a_s/m$ is the coupling strength, which is set by a_s. This parameter can be tuned with Feshbach resonances, although just to a certain point before leading to strong three-body losses. The particles also experience a trapping potential $V(\mathbf{r})$.

We apply a mean-field approximation by considering that the bosons are macroscopically occupying the same single-particle state, i.e., the many-body quantum state $|\Psi_N\rangle$ can be written as

$$\langle \mathbf{r}_1, ..., \mathbf{r}_N|\Psi_N|\mathbf{r}_1, ..., \mathbf{r}_N|\Psi_N\rangle \propto \psi(\mathbf{r}_1)...\psi(\mathbf{r}_N), \tag{19}$$

where ψ is normalized to N ($\int |\psi(\mathbf{r})|^2 d^3r = N$).

Under this assumption, the system can be described by the Gross-Pitaevski equation in 3D:

$$\left(-\frac{\hbar^2}{2m}\nabla^2 + V(\mathbf{r}) + g_{3\mathrm{D}}|\psi|^2\right)\psi = \mu\psi, \tag{20}$$

where $\mu \equiv \frac{\partial E}{\partial N}$ is the chemical potential.

Experimentally, we take our system into a 2D geometry by implementing a tight confinement along the vertical direction. Then, although the interactions preserve the 3D behavior, the motion of the atoms along the z direction is not allowed. In our experiment, this confinement is ensured by a harmonic potential, $V(z) = m\omega_z^2 z^2/2$. Assuming that the particles lie in the ground state of the harmonic potential, and that the energy necessary to go to the first excited state is larger than both the thermal energy and the interaction energy per particle, we can use the ansatz

$$\psi(\mathbf{r}) = \phi(x, y)\chi_0(z); \qquad \chi_0(z) = (\pi l_z^2)^{-1/4} e^{\frac{-z^2}{2l_z^2}}. \tag{21}$$

The condition of normalization now reads $\int |\phi(\mathbf{r})|^2 d^2r = N$; $\int |\chi_0(z)|^2 dz = 1$, and the in-plane density is $n(\mathbf{r}) = |\phi(\mathbf{r})|^2$.

By defining $g_{2\mathrm{D}} = g_{3\mathrm{D}} \int |\chi_0(z)|^4 dz$, the Gross-Pitaevski equation can be rewritten as

$$\left(-\frac{\hbar^2}{2m}\nabla^2 + V(\mathbf{r}) + g_{2\mathrm{D}}|\phi|^2\right)\phi = \mu\phi, \tag{22}$$

where now $V(\mathbf{r})$ represents the box potential: constant and equal to zero over the size of the sample and with sharp edges. Then, inside this box, the equation that describes the sample is

$$\left(-\frac{\hbar^2}{2m}\nabla^2 + g_{2\mathrm{D}}|\phi|^2\right)\phi = \mu\phi. \tag{23}$$

From the previous analysis, it has been found that the two-dimensional coupling strength when $l_z \gg a_s$ reads

$$g_{2\mathrm{D}} = \frac{\hbar^2}{m} \frac{\sqrt{8\pi} a_s}{l_z}. \tag{24}$$

Defining $\overline{g} \equiv m g_{2\mathrm{D}}/\hbar^2$, we get that the equation of motion can be rewritten as

$$\left(-\frac{\hbar^2}{2m} \nabla^2 + \frac{\hbar^2}{m} \overline{g} |\phi|^2 \right) \phi = \mu \phi. \tag{25}$$

Therefore, the coupling constant depends on the frequency in the quasi-2D regime as $\overline{g} \propto \sqrt{\omega_z}$.

B Efficiency curves of the AOM and AODs

In this Appendix, we analyze the power losses associated with the performance of acousto-optic deflector devices. Both AOMs and AODs have a central frequency at which the efficiency of first-order diffraction is maximized. Additionally, the RF frequency directly influences the diffraction angle. Therefore, as the operating frequency deviates from this central frequency, both the optical power of the first-order diffraction and the coupling efficiency decrease. Figure 18 represents the first-order and fiber coupling efficiency as a function of the RF frequency sent to the AOM.

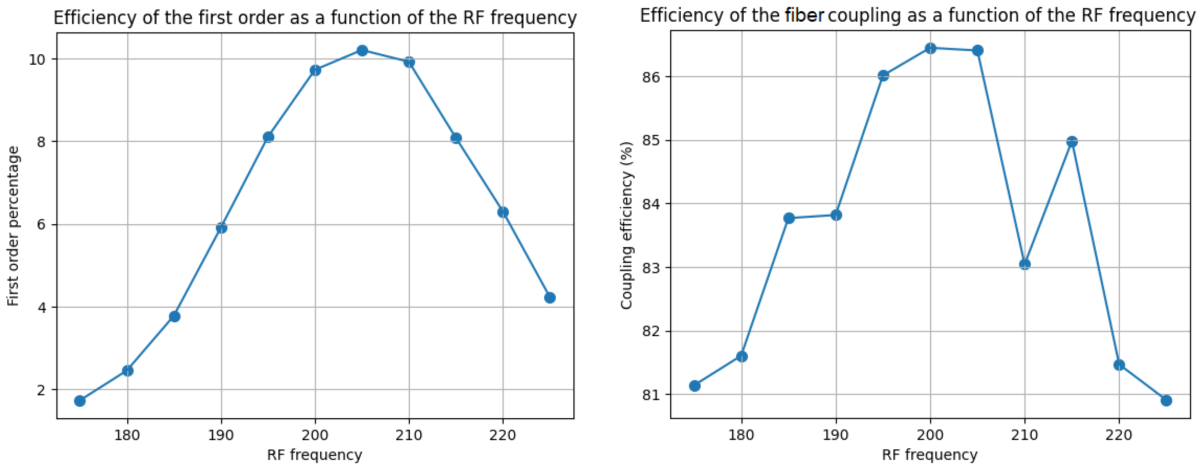

(a) (b)

Figure 18: Efficciency of the first order and of the fiber coupling for different RF frequencies in the case of the AOM.

The maximum efficiency is not achieved at the center frequency. Instead, the curve appears to be shifted away from the center. This shift is due to the increase in acoustic power with rising RF frequency. The VCO generates higher RF power at higher frequencies, which affects the efficiency of the first-order diffraction. The efficiency of the first order, η, is given by

$$\eta = \sin^2 \left(C \frac{\sqrt{P_a}}{\lambda} \right), \tag{26}$$

where P_a is the acoustic power and C is a constant depending on the characteristics of the AOM. It is measured with respect to the transmitted power, which, in this case, is 85.5% of the incident power. The efficiency increases with P_a until it reaches a *plateau*, beyond which it starts to decrease. In our case, the AOM is operating at its test frequency, which is below the point where the *plateau* is reached. Thus, the impact on the first-order efficiency from using a frequency slightly offset from the center is smaller than the effect of the increase in RF power. This is not the case for fiber coupling. As the frequency moves further from the center, the coupling efficiency decreases as expected due to changes in the diffraction angle.

For the AODs, the transmitted power was only 67% of the incident power. This is partly because the AODs are designed for a wavelength of 1064 nm rather than 675nm. Since the AODs could be absorbing part of the optical power coming out of the laser, it is necessary to be cautious with the incident power levels to avoid damaging the AODs.

In this case, we measured the efficiency of the 1-1 order while varying the RF frequency in different ways. In Figure 19, *Vertical* (or *Horizontal*) indicates that the RF frequency of the vertical (or horizontal) AOD was adjusted while the other AOD's frequency was held at the center frequency. In the cases of *Both*, the RF frequencies of the two AODs were the same.

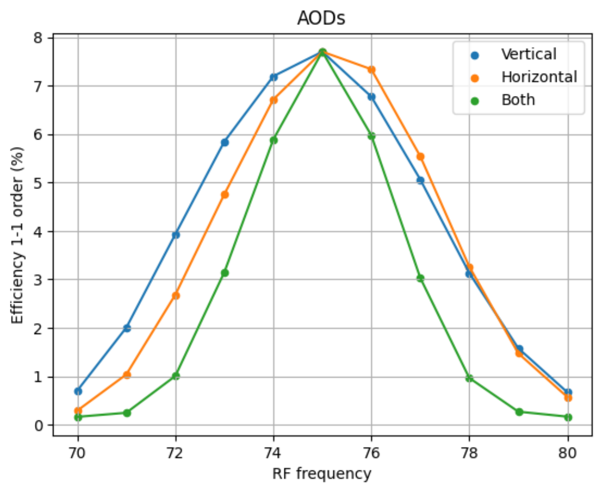

Figure 19: Efficiency of the 1-1 order of the 2D AODs.

As expected, the efficiency decreases more rapidly when varying the frequency of both AODs simultaneously compared to when it is changed only for one AOD. This more pronounced reduction in efficiency occurs due to the compounded effects of frequency shifts on both devices.

This analysis provides a relevant insight for integrating these acousto-optic deflector devices into the final experiment to homogenize the beam profile for the potentials. However, none of the setups proved suitable under the test conditions due to the low power efficiency observed in both cases.

C Analysis of the possible fitting functions

In this Appendix, we explore various fitting models for the PSF to determine which one most accurately reproduces the original image. We focus on three 2D functions: an asymmetric Gaussian, an asymmetric Airy disk, and the theoretical PSF of a square aperture. The latter is mathematically described by

$$\mathrm{PSF}(x, y) = (\mathrm{sinc}(\alpha_x x))^2 \ (\mathrm{sinc}(\alpha_y y))^2 , \tag{27}$$

where α_x and α_y correspond to the free parameters for the fit.

Since the size of a micromirror is comparable to the resolution of the imaging system, the image of a micromirror may be present in the PSF. To account for this, we convolve each of these functions with the image of a micromirror, modeled as a square rotated by 45° with a side length s_{fit} given by

$$s_{\mathrm{fit}} = \frac{s_{\mathrm{mirror}} \cdot d}{p}, \tag{28}$$

where $s_{\mathrm{mirror}} = 7.6\mu\mathrm{m}$ is the side of the micromirror on the DMD, d is the demagnification, and $p = 3.45\mu\mathrm{m}$ is the size of a pixel in the camera. Figure 20 displays these different fits for the PSF with highest Strehl ratio.

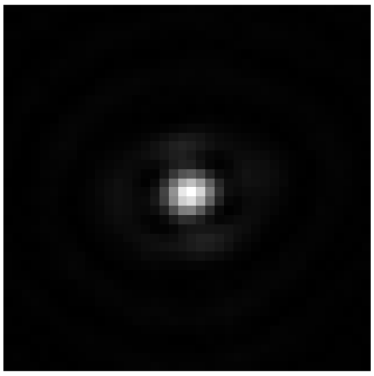

(a) Original PSF.

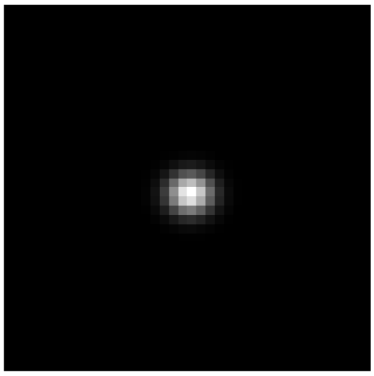

(b) Asymmetric Gaussian.

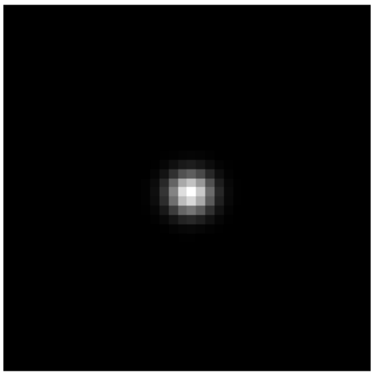

(c) Asymmetric Gaussian convoluted with a rotated square.

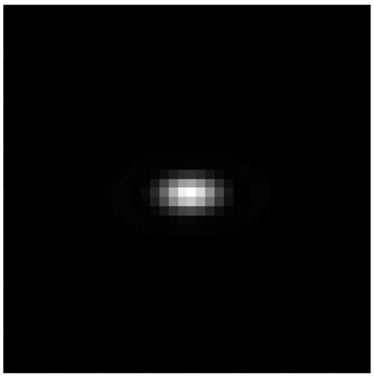

(d) Asymmetric Airy disk convoluted with a rotated square.

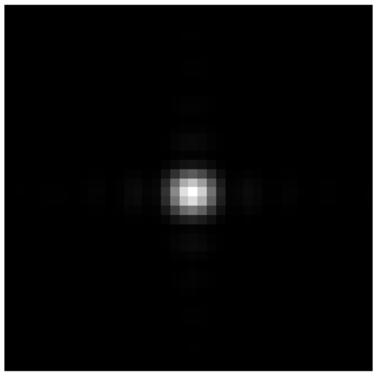

(e) Product of sinc functions convoluted with a rotated square.

Figure 20: Different fits.

Since s_{fit} is approximately 1.7 pixels, the difference between the Gaussian and the convolved Gaussian fits is not visually apparent. The sinc function fit partially captures some features of the halo surrounding the main peak, while the Airy disk fit does not succeed in this regard. For a more detailed analysis, the logarithmic scale of these images is shown in Figure 21.

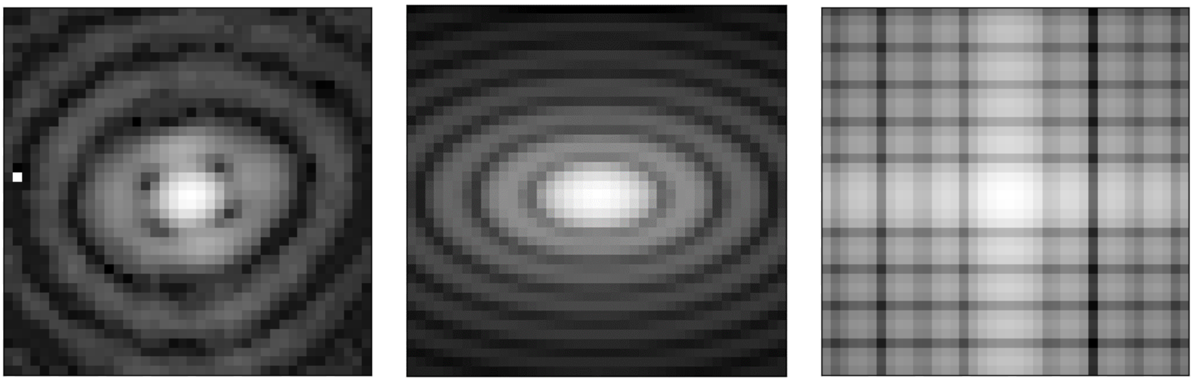

(a) Original PSF. (b) Asymmetric Airy disk. (c) Product of sinc functions.

Figure 21: Logscale for different fits.

From these images, we conclude that neither the Airy disk nor the sinc function accurately represent the shape of the PSF. This suggests that the halo surrounding the main peak is primarily due to optical aberrations. Given that these models cannot reproduce the PSF accurately and considering their complexity, we choose to use the 2D Gaussian model.

Finally, to assess the difference in resolution when fitting with a 2D Gaussian compared to the convolved 2D Gaussian, we extract the fitted PSF width and calculate the resolution with the relation $R = 2.905\sigma$. Using the periodic pattern of one micromirror used in Section 5, we consider a larger dataset for comparison. The values for the resolution obtained with the two fits are plotted as a function of the distance from the center of the pattern in Figure 22.

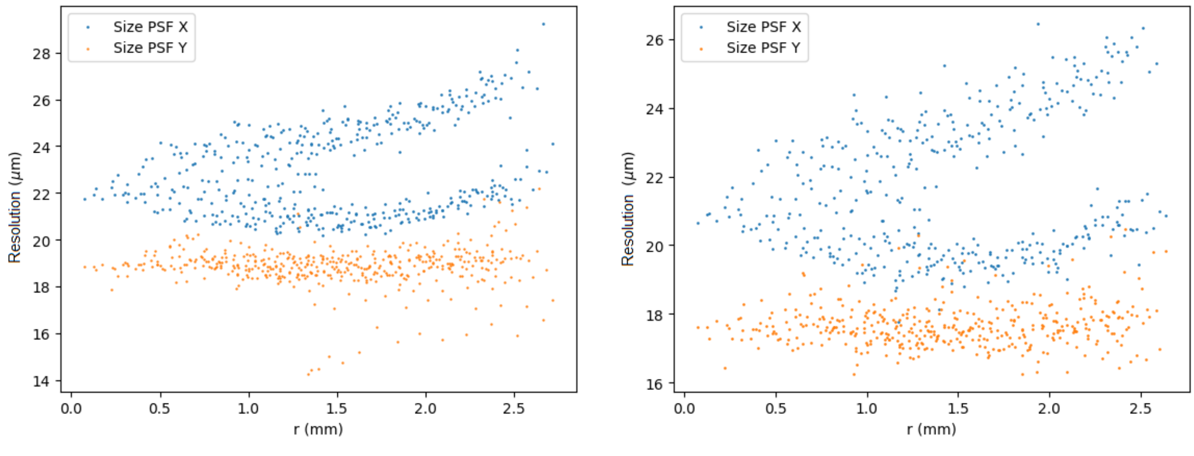

(a) Fit with a gaussian. (b) Fit with a gaussian convoluted with a rotated square.

Figure 22: Widths of the PSF obtained from the fitting process as a function of the distance to the center of the pattern.

Although less successful fits are obtained with the convolution, the values of the resolution are smaller than for the Gaussian. This indicates that incorporating the micromirror image into the PSF results in a resolution closer to the expected value. Consequently, we use this convolution as a fitting function.